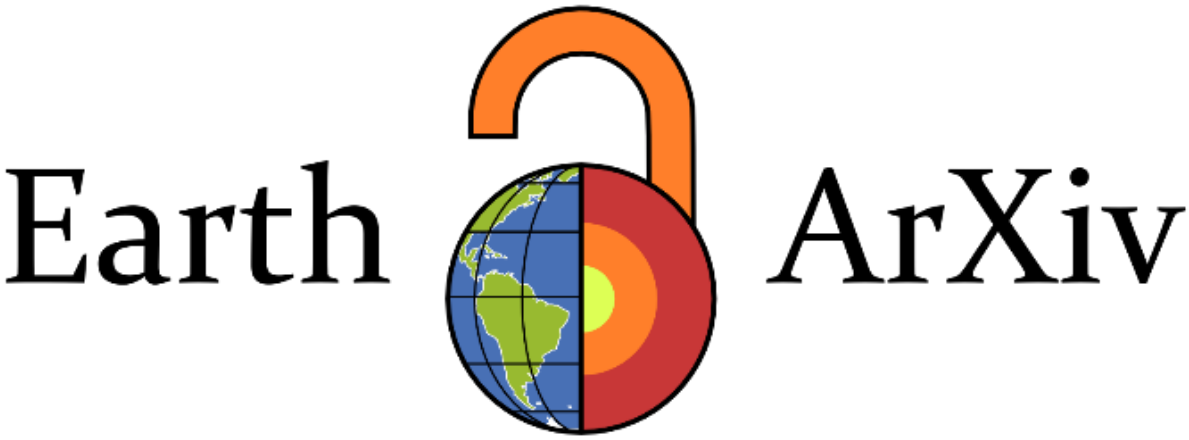

Causal analyses reveal changing land-atmosphere patterns and soil moisture control under warming

Dian Indrawati[1,2], Somnath Mondal[1*], Poulomi Ganguli[3], Auroop R. Ganguly[1*]

[1*]Department of Civil and Environmental Engineering, Northeastern University, 360 Huntington Ave, Boston, 02115, MA, US.
[2]Department of Civil Engineering, Jenderal Achmad Yani University, Terusan Jend. Sudirman, Cimahi, 40531, West Java, Indonesia.
[3]Department of Agricultural and Food Engineering, Indian Institute of Technology Kharagpur, Kharagpur, Kharagpur, 721302, West Bengal, India.

*Corresponding author(s). E-mail(s): s.mondal@northeastern.edu; a.ganguly@northeastern.edu;
Contributing authors: dian.indrawati@lecture.unjani.ac.id; poulomizca@gmail.com;

Abstract

Climate change is projected to modify the global water cycle and land-atmosphere interactions. However, warming-induced changes in multivariate dependence remain insufficiently explored. Here we examine the interdependence among temperature, precipitable water, precipitation, evaporation, soil moisture, and runoff in all five earth system models within the latest IPCC CMIP6 ensembles that generate relevant simulated data. Our causal network analyses, augmented by artificial intelligence, suggest a near universal statistically significant shift in interdependence structures, along with a growing role of soil moisture, under mid- and end of century scenarios, including pronounced regional and seasonal heterogeneity. Our results have implications for food security, including a 3% decline in global domestic production and 8% in the northern subtropics. Our findings motivate reliable observations and credible early warning systems.

Keywords: Interdependence, Soil moisture, Climate change, Artificial intellegence

1 Main

Climate change is altering the global water cycle, exacerbating both droughts and floods[1]. Historical examples include "Day Zero" water crisis in Capetown, South Africa (2017-2018)[2], as well as intensifying extreme precipitation and consequential detrimental floods in the United States (1980-2024)[3]. Future projections are even more alarming, with declining discharge in major rivers worldwide[4] alongside increasingly unprecedented flooding events by the end of the twenty-first century[5]. These crises are consistent with broader observational evidence and the underlying science that rising temperatures (T) shift the mean and variability of atmospheric and land variables that exhibit hysteresis or practical irreversibility[6]. Since energy and moisture circulation couples these variables, warming does not only shift variables independently but also their interdependence, often nonlinearly[7].

Fig. 1a schematically shows warming-induced shifts in annual mean and variability of hydroclimatic variables at the *mid-* (2021-2050) and *end of century* (2071–2100) periods relative to the baseline (1971-2000). However, these projections capture only marginal behavior, leaving their multivariate interactions unexplored[8, 9]. This is a crucial gap since warming may modify the regional topology of the global water cycle[1, 10–12]. Such modification, typically characterized through dependence analysis[13], are also the mechanistic pathways of intensifying compound extremes [14]. Furthermore, how changes in hydroclimatic dependence culminate in extreme events may have seasonal and regional heterogenity. For instance, land-atmosphere feedbacks under warmer summer conditions can pose serious drought and atmospheric aridity[15, 16] through positive (i.e. -dry spring and dry summer) or negative couplings (wet spring and dry summer)[9, 17–19]. In contrast, simultaneous increases in atmospheric and surface water (early melting or rain on snow events) during the cooler winter season can intensify not only flooding events[20], but can also trigger latent heat-driven anomalous winter warming, such as recent Boston heatwaves[21]. Furthermore, changes in hydroclimatic dependence can also affect agriculture, as crop yields rely on net water availability and soil-evapotranspiration coupling (necessary for plant respiration) to meet water needs for growth and maturity[22]. To our knowledge, linking such multivariate dependence changes to direct regional crop productivity as well as regional economic output has not been addressed in previous studies.

Nevertheless, previous studies typically consider only limited subsets of variables, therefore, cannot distinguish between the competing mechanistic pathways through which hydroclimatic interdependence operates. Fig. 1b illustrates how soil moisture can influence precipitation through at least two distinct pathways[23]: (1) dynamic: SM-induced surface heating [24] generates thermal lows that drive moisture convergence from remote sources (i.e., monsoon), and (2) thermodynamic: local evaporation [23] directly supplies boundary-layer moisture that fuels convection. These pathways likely show opposite signs of soil moisture-precipitable water coupling: negative under dynamic dominance and positive under thermodynamic dominance. Similarly, soil moisture-temperature pathway can also show different regime depending on whether the system is in water-limited or energy-limited state[25]. Yet, recent studies also have not assessed whether warming may shift regional hydroclimatic interdependence system from one pathway to another.

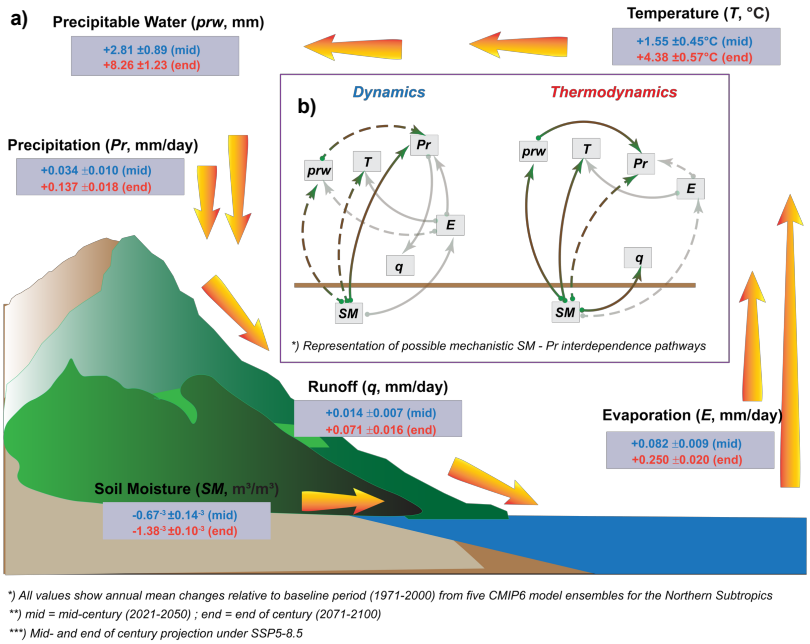

Fig. 1 Global warming drives regional shifts in mean, variability and interdependence of hydroclimatic variables and the water cycle. a) Spatial changes in mean and variance among hydroclimatic variables during the mid- (2021-2050) and end of century (2071-2100) relative to the baseline period (1971-2000); b) Competing interdependence pathways among hydroclimatic variables.

The objective of the present study was to address these questions: (1) how does global warming scale regionally to influence changes in the mean, variability, and interdependence of hydroclimatic variables including temperature (T), precipitable water (prw), precipitation (Pr), evaporation (E), soil moisture (SM), and runoff (q)? (2) how do these multi-dimensional changes alter global water stress, as exemplified by impacts on crop yield risk and regional economic output? Hence, we quantify the sensitivity of hydroclimatic variables to global and regional warming and characterize their interdependencies using linear and nonlinear dependence approaches. Established dependence measures (i.e., rank correlations, or mutual information) can quantify the strength and structure of associations but do not decompose variable-specific contributions or assign causal directionality to interactions within a multivariate system[13]. Granger causality (GC)[26] assesses directed temporal dependencies but assumes linearity, and therefore can not capture nonlinear components of hydroclimatic interdependence that arise from threshold behaviour, regime transitions, and saturating feedbacks[9, 25]. As such, we complement linear GC with a deep learning (DL) based Random Forest[27] combined with SHapley Additive exPlanations (RF-SHAP)[28]. Here, RF-SHAP uses interpretable framework to evaluate the non-linear strength and direction of predictive contributions. Finally, to demonstrate impact relevance, we quantify how shifts in the mean, variability, and interdependence of hydroclimatic variables influence regional crop production using restricted cubic splines (RCS)[29].

In addition, economic impacts on country-level gross domestic product (GDP) are assessed through empirical dose–response functions[30].

We use Coupled Model Intercomparison Project Phase 6 (CMIP6)[31] output from five Earth System Models (ESMs) that have all hydroclimatic variables considered in this analysis and include two contrasting emission pathways (SSP1-2.6 and SSP5-8.5)[32]. The globe is delineated into five primary climate regions[33, 34]: tropics (TROP, 23.5° N–23.5° S), subtropics (northern subtropics:NSZ, 23.5°–35° N and southern subtropics:SSZ, 23.5°–35° S), and midlatitudes (northern midlatitudes:NMZ, 35°–60° N and southern midlatitudes:SMZ 35°–60° S). Each zone captures major atmospheric circulation regimes[35] and appears to be governed by a distinct dominant coupling among hydroclimatic variables (e.g., soil moisture-precipitation feedbacks dominate in the tropics[23]). Separating the Northern and Southern Hemispheres further accounts for hemispheric asymmetries in land–ocean distribution and radiative forcing[36].

1.1 Spatiotemporal modulation of hydroclimatic variables to global and regional warming

We first analyse the sensitivity of hydroclimatic variables to global mean surface temperature (GMST) for the *mid-* (2021–2050) and *end of century* (2071–2100) relative to the 1971–2000 baseline (See Methods). Here, shifts in GMST are categorized within the framework of the Intergovernmental Panel on Climate Change (IPCC) thresholds (<1.5°C, 1.5–2°C, and >2°C), to systematically assess projected warming versus the stabilization targets agreed under the 2015 Paris Agreement[37]. A 1:1 reference line is included for temperature assessment, where values falling below or above the line indicating deviations in the scaling of regional mean surface temperature (RMST) relative to GMST. We subsequently quantify the regional changes in the mean and variability of hydroclimatic variables from CMIP6 model ensembles, then relate them to changes in GMST (See Methods). A consistency check of the CMIP6 data has been done against the European Center for Medium-Range Weather Forecasts Reanalysis version 5 (ERA5) datasets[38] for the *early century* (1981-2010) relative to baseline (See Methods).

CMIP6 projections show that *mid-century* GMST clusters around 1.5°C with some overlap between SSP1–2.6 and SSP5–8.5 (Fig. 2a-c), but by the *end of the century* the scenarios diverge, with SSP1–2.6 and SSP5–8.5 staying in between 1.5°C to 2°C and exceeding 2°C respectively (Fig. 2d-f). In TROP, warming closely tracks the 1:1 reference line, suggesting equal increase in annual RMST with increase in GMST (Fig. 2a,d), consistent with efficient heat redistribution by frequent deep convection [39]. However, non-tropical regions show marked hemispheric asymmetry, with NSZ (4.55°C) and NMZ (5.99°C) warming at up to two to three times the global mean (3.37°C), whereas warming in SSZ (2.10°C) and SMZ (1.37°C) is comparatively weaker than GMST change across models and scenarios during JJA and DJF (Fig. 2b,c,e,f). Stronger warming in the Northern Hemisphere may reflect differences in greenhouse gas concentrations[40] and the greater land fraction, given that land surfaces warm faster than oceans[41]. Interestingly, increases in variability of RMST is much higher

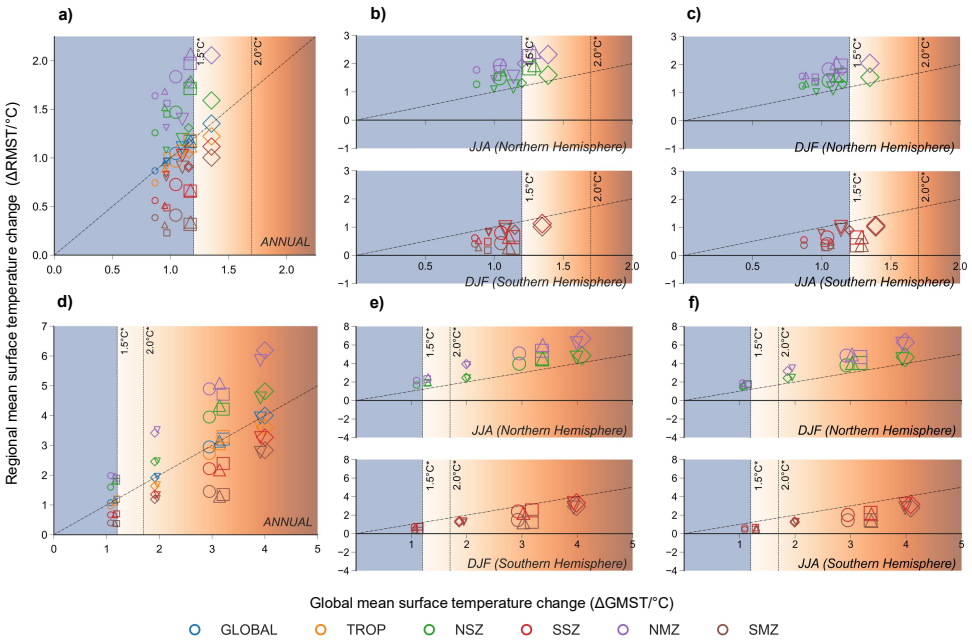

Fig. 2 Multiple IPCC's tresholds reveal global mean surface temperature (GMST) promotes regional mean surface temperature (RMST) in non linear but systematic patterns. Sensitivity of regional temperature to GSMT across: a, b, c) mid- (2021–2050); and d, e, f) end of century (2071–2100) periods, relative to the 1971–2000 baseline. The x-axis represents changes in GMST (°C), with y-axis shows corresponding changes in RMST. Panel a,d) annual results corresponding to all regions; b,e) summer and c–f) winter corresponding to subtropics and midlatitudes regions. The vertical reference lines equivalent to the 1.5 °C and 2.0 °C warming relative to pre-industrial level as defined in IPCC reports. Marker shapes represent CMIP6 Global Climate Models: circle (MIROC6), triangle (NorESM2-LM), square (NorESM2-MM), diamond (CMCC-CM2-SR5), inverted triangle (CMCC-ESM2), and pentagon (ERA5). Marker size indicated the emissions scenario (SSP1-2.6: small; SSP5-8.5: large). The 1:1 reference line is representing an idealized relationship in which a 1 °C increase in GMST corresponds to 1 °C increase in RMST. See Supplementary 1 for remaining results.

than in its mean (Fig. 3; Supplementary 2 and 3) over *mid-* (μ_T: 0.53–0.54%, σ_T: 55–87%) and *end-century* (μ_T: 1.41–1.52%, σ_T: 128–139%) during JJA and DJF. This indicates an elevated probability of both extreme cold and heat events in these regions.

Prw closely tracks $RMST$ (Fig. 2; Fig. S1 Supplementary 1), with hemispherically asymmetric but uniformly positive changes consistent with thermodynamic increases in column water vapor under warming and near-constant large-scale lower-tropospheric relative humidity[42, 43]. Prw increases more strongly at seasonal than annual timescales in non-tropical regions with stronger sensitivity in NSZ and NMZ (8–13% per °C) and weaker sensitivity in SSZ and SMZ (3–4% per °C); similar to $RMST$, it exhibits larger changes in variability than in the mean (Supplementary 2 and 3). However, increases in prw do not necessarily translate into higher Pr, as prw contributes to Pr only when atmospheric and land-surface conditions are favorable for

condensation [44]. Accordingly, Pr exhibits a more heterogeneous response pattern to GMST than prw (Fig. S2 Supplementary 1). In particular, while Prw increases over time, Pr in SSZ during JJA and in the NSZ during DJF show declines, likely associated with Hadley cell expansion, a poleward shift of subtropical dry zones enhancing aridity [45, 46]. In contrast, E increases faster than Pr, producing the largest net water deficits in the SSZ, especially in JJA, where stronger evaporation and variability indicate heightened seasonal water scarcity, while the greater changes in annual than seasonal variability in Pr suggests larger changes in spring or autumn (Fig. 3; Supplementary 1-3).

SM declines across all regions and seasons during both the *mid-* and *end of century*, most strongly in the NMZ, as enhanced net radiation increases evaporative demand so that E offsets or exceeds Pr, causing SM losses in regions with increased Pr[47]. Although previous studies have reported that SM and q are highly correlated[20], shifts in both variables differ with NSZ and NMZ exhibit the strongest q modulation during JJA and DJF (Fig. S4-5 Supplementary 1), likely associated with vegetation than with warming [48, 49]. The variances of both SM and q also diverge across spatiotemporal settings (e.g., SM: $\Delta\sigma_{\mathrm{DJF}} = -2.42\%$; and q: $\Delta\sigma_{\mathrm{DJF}} = 51.46\%$)(Fig. 3; Supplementary 2 and 3).

1.2 Warming driven modulation in hydroclimatic dependence

We examine changes in hydroclimatic interdependence during *mid-* and *end of century* periods in the JJA subtropics (NSZ, SSZ) and DJF midlatitudes (NMZ, SMZ), where the largest hydroclimatic shifts occur (P–E deficits in subtropics and SM declines with increase in q in midlatitudes). Using graphical networks from GC and RF–SHAP (Fig. 4; Supplementary 4), we classify variables as dominant drivers and dependent variables, each influencing and being influenced within the system[48, 50, 51]. Meanwhile, we term variables which both causally drives and get driven by other variables as super-nodes (network hubs)[52]. To ensure robust detection, we constrain lag structure and apply significance thresholds (GC: $p < 0.05$; RF–SHAP: $\mathrm{D}_V > 0.015$), reporting only relationships supported by at least two of five CMIP6 models[28, 53–55]. In RF-SHAP analysis, positive predictive influence indicates that source variable increase prediction of the target variable, whereas a negative predictive influence indicates suppression (see Methods). Land–atmosphere interactions are defined as linkages between atmospheric (T, prw, Pr) and land-surface variables (E, SM, q), including both one-way coupling and feedbacks[25].

During JJA across subtropics, linear GC primarily detects directional causal dependence among atmospheric variables and, to a limited extent, land–atmosphere interactions (Fig. 4; Supplementary 4; Table S1 Supplementary Table). Toward the *end of century*, the NSZ shows emergent $SM \rightarrow$ q coupling (Fig. 4c,d), with SSP1-2.6 additionally indicating $SM \rightarrow$ Pr, whereas the SSZ remains more heterogeneous (Fig. 4e-h; Supplementary 4), with scenario- and period-dependent reversals between prw $\rightarrow$ pr and $SM \rightarrow$ prw that point to shifting dominance between atmospheric moisture control and land–atmosphere coupling. By contrast, DJF midlatitudes show few robust causal links (Supplementary 4; Table S1), with only limited, scenario-dependent signals—mainly (prw $\rightarrow SM$) in the NMZ and ($q \rightarrow$ prw) or ($T \rightarrow$ pr)

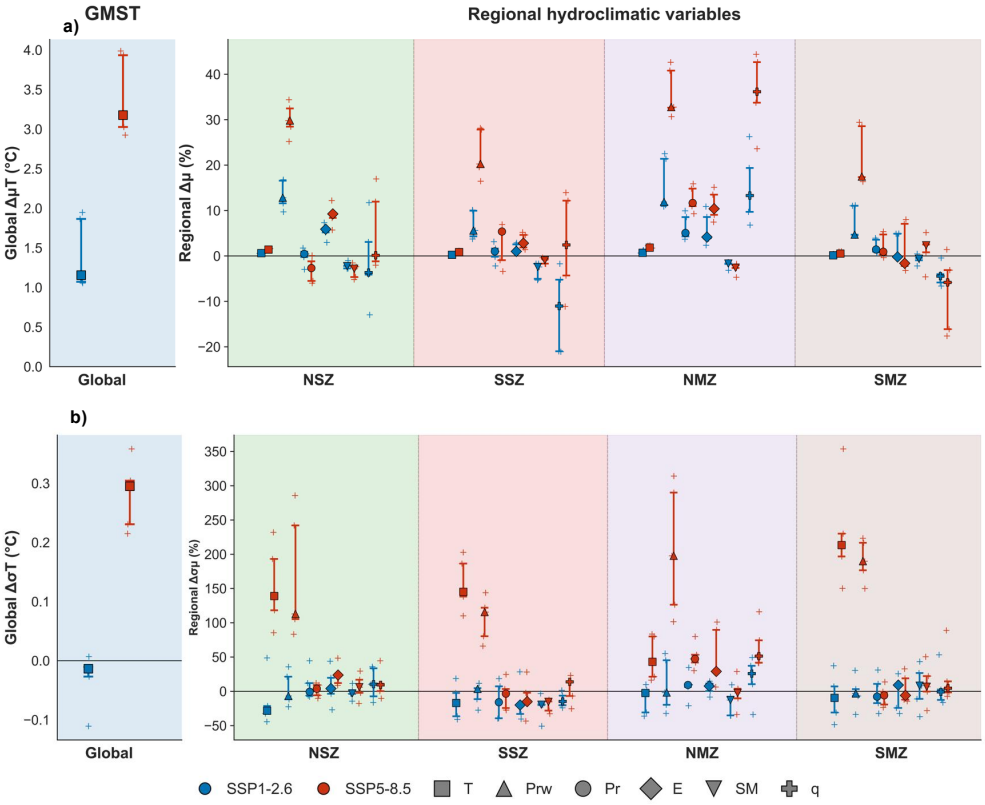

Fig. 3 Warming-induced modifications in the mean and variability of hydroclimatic variables. Changes in a) mean; and b) variability of hydroclimatic variables during DJF season across non-tropical regions at *end of century* (2071–2100) relative to the baseline (1971–2000) periods from CMIP6 model ensembles. Region colors are consistent with Fig. 2. See Supplementary 2 and 3 for remaining results.

in the SMZ under SSP5–8.5 indicating weak hydrological–atmospheric coupling and thermodynamic control of Pr [50, 56]. Overall, GC shows large inter-model spread (agreement <50%) and limited ability to resolve the full spectrum of land–atmosphere interactions.

In contrast, RF–SHAP performs desirably with substantially higher inter-model agreement (60–100%). During JJA, SM emerges as the dominant driver, although its effects on other variables vary by region, period, and scenario (Fig. 4; Supplementary 4; Table S1 Supplementary Table). Over the NSZ, SM exerts a consistent negative predictive influence on T, with weak to strong significance ($D_V > 0.015$ to > 0.03) similar to established soil-temperature coupling [25]. During *mid-century*, SM negatively influences prw but positively influences Pr regardless of scenario, whereas by the *end of century* its influence on prw and q becomes consistently positive whereas effect

on Pr shifts from negative (SSP1-2.6) to positive (SSP5-8.5), suggesting an increasing role of SM in enhancing moisture supply for Pr [22]. Interestingly, E emerges as a dominant driver alongside SM, exerting a consistent negative influence on T, prw, and Pr during *mid-century* under SSP1-2.6 and by the *end of century* under SSP5-8.5. Contrasting effects of SM and E on Pr suggest that stronger radiative forcing shifts NSZ dynamics from soil-moisture memory toward soil–water–atmosphere exchange, while direct $SM - E$ coupling remains weak, likely due to differences in the memory timescales of E and SM under summer dry conditions[57]. Over the SSZ, SM shows period-dependent but broadly scenario-consistent effects (Supplementary 4; Table S1 Supplementary Table), with positive predictive influences on prw and Pr throughout, a positive influence on E during *mid-century* that reverses by the *end of century*, likely reflecting a shift in soil moisture–evaporation coupling under changing SM regimes[22].

In coupled land–atmosphere systems, feedbacks among surface and atmospheric fluxes through both reinforcing and damping pathways[50]. Across the subtropics, T, prw, Pr, and q emerge as super-nodes, with the NSZ shifting from prw- to Pr-dominated coupling and the SSZ remaining T-dominated under SSP5-8.5. Please note that prw consistently enhances T and Pr but suppresses E over both NSZ and SSZ, underscoring strong atmospheric control on subtropical hydroclimate (Fig. 4; Supplementary 4; Table S1 Supplementary Table). During DJF in the midlatitudes, SM is the dominant driver of hydroclimatic coupling, generally suppressing T in the NMZ except for emergent positive SM–T coupling by the *end of century* under SSP5–8.5, consistent with earlier findings for similar regions[16, 19]. SM consistently enhances Pr, exerting scenario-dependent control on E. Over SMZ, by the *end of century*, SM exerts positive effects on prw, Pr, and occasionally T indicating strong soil moisture–atmosphere coupling[16, 25].

Across midlatitudes, E appears as a dominant driver across NMZ during *end of century* under SSP1-2.6, along with during *mid-century* under SSP1–2.6 and by the *end of century* under SSP5–8.5 across SMZ (Supplementary 4; Table S1 Supplementary Table). In these regions, enhanced E coincides with reduced local atmospheric moisture ($E \Rightarrow \text{prw} \downarrow$) but increased precipitation ($E \Rightarrow \text{Pr} \uparrow$), indicating weaker vertical moisture but stronger horizontal moisture transport and convergence within the atmosphere[11]. At *mid-century* under SSP1-2.6, T acts as a super-node in the NMZ by increasing prw while suppressing Pr, whereas by the *end of century* under SSP5-8.5, Pr becomes the dominant driver of T, prw, and q, indicating strengthened winter moisture coupling[20]. Unfortunately, no dominant driver is detected at *mid-century* under SSP5–8.5 due to insufficient model agreement.

Comparing *mid-* and *end of century* interdependencies reveals difference in GC and RF-SHAP estimations (Supplementary 5). GC predominantly detects a net loss of connections in the NSZ (50–54%) but net emergence in the SSZ (42–50%). RF-SHAP highlights structural reorganization such dominant sign reversals (i.e., shift from $SM - Pr$ positive to negative coupling across NSZ during JJA) and shifts in interaction strength (i.e., weaken of $SM - T$ coupling across NMZ during DJF) rather than simple topological change, particularly across the subtropics (58–67%) and NMZ

(52–55%). Across both methods and all zones, about 90% of interdependence is modified, with more than two-thirds of changes involving $SM - Pr$, SM–T, and SM–E couplings, along with pronounced regional and seasonal heterogeneity. This validates our inherent assumption that land–atmosphere coupling will be strongly nonstationary under warming, in both the direction and magnitude of feedbacks.

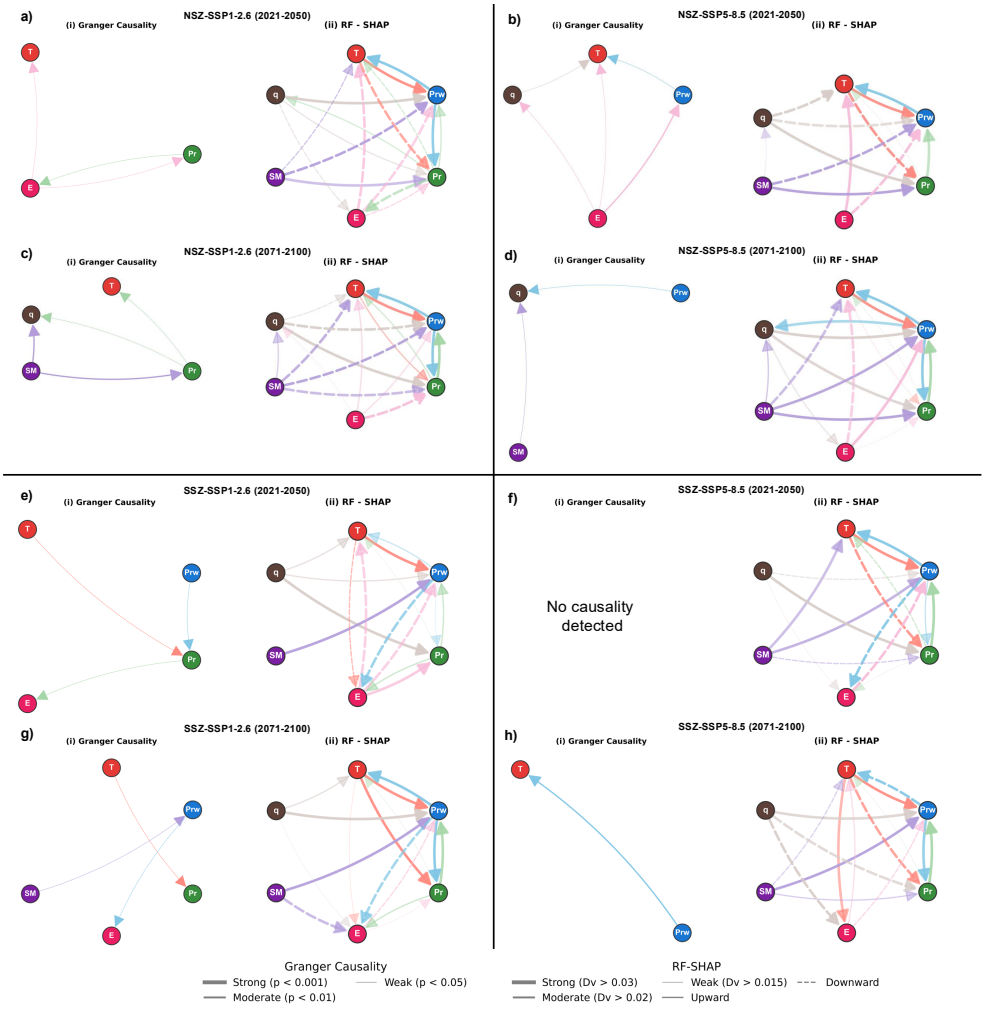

Fig. 4 AI-augmented causal dependence analyses reveal changing interdependence among hydroclimatic variables due to warming. Regional interdependence during JJA season for NorESM2-LM across: a–d) NSZ region under a) SSP1-2.6 mid-century, b) SSP5-8.5 mid-century, c) SSP1-2.6 end of century, d) SSP5-8.5 end of century; e–h) SSZ region under e) SSP1-2.6 mid-century, f) SSP5-8.5 mid-century, g) SSP1-2.6 end of century, h) SSP5-8.5 end of century. See Supplementary 4 for remaining results.

1.3 Projected impacts of multivariate hydroclimatic shifts on regional rice and maize productivity and GDP

Here we examine how multivariate characterization of E and SM as one of prominent dominant drivers (see previous section) which also govern root-zone water status and stomatal regulation, the primary determinant of plant growth under water stress[29, 58] translate into crop productivity. We choose rice and maize since they are two of the most widely produced crops globally[59] and exhibit contrasting water requirements, cultivation systems, and stress sensitivities[58]. Accordingly, we plot in parallel yield productivity as a function of changes in mean, variability and interdependence of E and SM along with the net available atmospheric water ($P - E$) as a proxy for green water availability[12, 60] and $E - SM$ interdependence. We then assess how resulting yield changes affect country-level GDP(see Methods).

We found that rice and maize exhibit strikingly contrasting responses across climate regions. Rice productivity declines by 10.2–35.8% across the regions, except SMZ with increase of 10.16% (Fig. 5a). Maize, conversely, displays a regional increase of 12.1–54.4% across regions with SMZ showing 18.9% reduction (Fig. 5b) consistent with previous observations[29, 61]. Further analysis shows that E–SM dependence is negative only in TROP (-0.12) and positive elsewhere (0.01–0.16), while water availability ($\Delta P - E$) declines most strongly in TROP, NSZ, and SSZ (-0.04, -0.09, and -0.24 mm), linking shifts in the mean, variability, and interdependence of SM and E to crop productivity and extending earlier evidence that T, SM, and crop water supply govern yield variability in maize, soybean, and sorghum [29, 62]. Finally, these yield shifts are projected to reduce GDP across all regions, with the most severe impacts in NSZ countries (-7.72% of GDP; e.g., Bangladesh, Egypt and Mexico) and milder impacts in SMZ countries (-0.82% of GDP; e.g., Australia, Chile, and Argentina) (Fig. 5c).

2 Discussion

This study provides a framework for assessing how global warming scales regionally and seasonally in terms of hydroclimatic system behavior by characterizing long-term changes in mean, variability and especially the interdependence structure of the hydroclimatic variables. Several conclusions emerge, some well known[16, 23, 25, 40, 43, 60] (see Table S2 Supplementary Table). First, variance shifts exceed mean shifts in atmospheric and flux variables (T, prw, Pr, E), whereas land variables (SM, q) show comparable mean and variance changes. Second, thermodynamic scaling is hemispherically asymmetric, with northern and southern non-tropical regions exhibiting super- and sub-Clausius–Clapeyron behavior, respectively. Third, warming modifies more than 90% of interdependence structures between *mid-* and *end of century*, with SM accounting for over two-thirds of these changes through its links to T, Pr, and E.

The role of SM emerges clearly in non-tropical regions through impact-relevant shifts in dependence structure: in the NSZ during JJA, *mid-century* negative SM–prw but positive SM–Pr dependence indicates a domaination of dynamic pathway in which SM affects Pr through circulation-driven (i.e. -thermal low) moisture convergence rather than local recycling ($E - prw$ dependence is negative). By the *end of century* positive SM–prw and negative SM–Pr dependence suggests a transitional

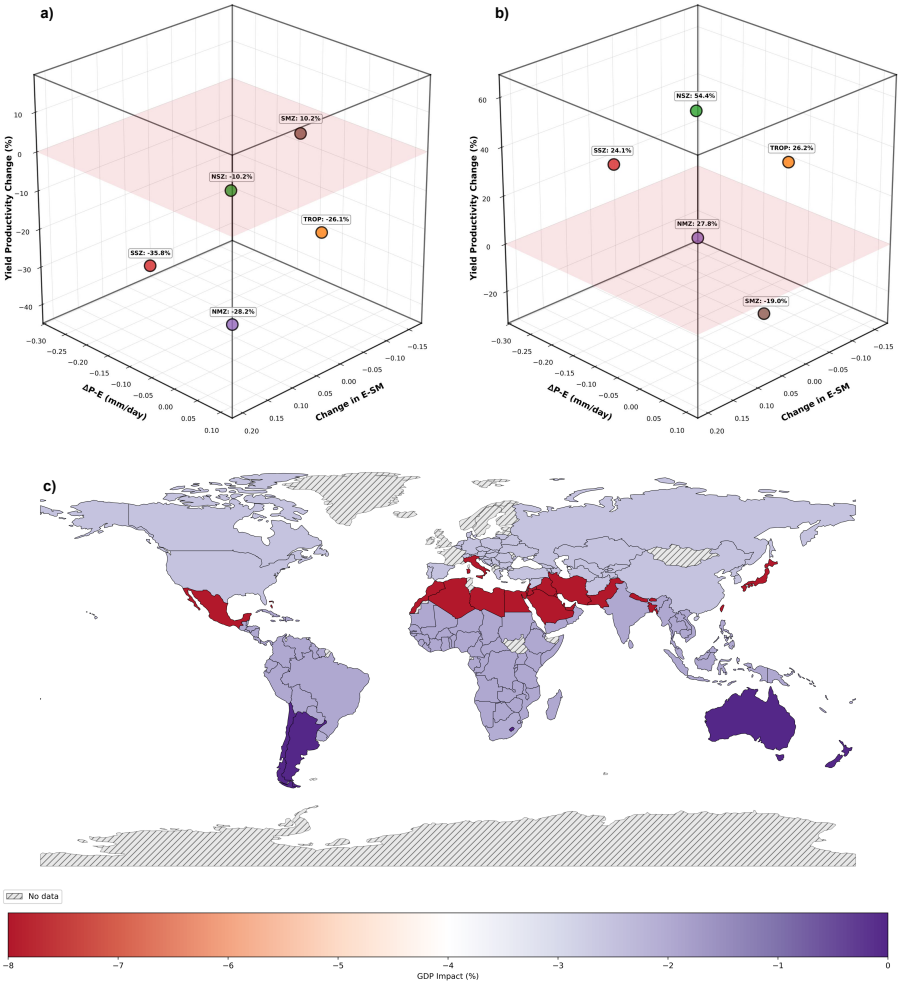

Fig. 5 Implications of shifts in mean, variability and interdependence of dominant drivers to global food productivity and gross domestic product (GDP) due to warming. Effects of multidimensional shifts of E and SM on regional a) rice productivity; b) maize productivity; and c) country-level GDP. The results across five model ensemble toward end of century (2071-2100) under SSP5-8.5 scenario relative to early century (1981-2010). Legend definitions in a) and b) are consistent with Fig. 2

thermodynamic regime with shift from "moisture export" to "moisture retention," but in a transitional state with available moisture is not efficiently converted to Pr. Under SSP5-8.5, this shifts further to positive SM–Pr, marking a fully coupled positive feedback regime in which intense surface heating overcomes convective inhibition and can favor local moisture convergence. Such positive feedbacks amplify hydrological extremes bidirectionally, where dry (wet) conditions intensify via rapid SM depletion (increase in SM and recycled Pr) with examples including 2021-22 Northeast US drought [19].

In contrast, during DJF in the NMZ, SM–Pr coupling remains positive under both scenarios by the *end of century*, while SM–T coupling reverses from negative to positive under SSP5-8.5, indicating wetting-driven warming likely mediated by water vapor driven enhancement of *downward* longwave radiation (greenhouse trapping). Over the SSZ, despite weaker warming than in the NSZ and NMZ, pronounced declines in SM and Pr during JJA reverse the SM–E relationship from positive to negative, suggesting decoupling of soil moisture and evaporation that may disrupt the canonical SM–E–Pr recycling pathway [63], with potential consequences for vegetation water stress and terrestrial carbon uptake [18]. Targeted land-surface experiments are needed to confirm this transition and identify the critical SM threshold for sign reversal.

In the SSZ, the diminished role of SM is consistent with the emergence of prw and T as *end-of-century* super-nodes, indicating stronger atmospheric control of hydroclimatic variability. The sign of $q \rightarrow T$ reverses between zones with NSZ, $(q \rightarrow T)$ showing negative predictive relationship whereas in SSZ it shows positive reflecting summer-winter contrast. In the NSZ (summer), q suppresses T via enhanced evaporative cooling. In contrast, in the SSZ during winter, q elevates atmospheric moisture (positive $q - prw$ relationship), strengthening the water-vapor greenhouse trapping and enhancing downward longwave radiation, producing net warming rather than the cooling seen in summer.

These projected changes have far-reaching implications for water availability, drought and flood adaptation, energy production, and food security. We specifically demonstrate how these altered dynamics propagate into cereal production, with cascading effects on national economic performance. As a result, rice productivity risk dominates across all regions, with NSZ having the highest GDP loss by the *end of century*. Here, please note that the current study has caveats, including possible masking of local processes by broad regionalization, as well as uncertainties in soil moisture observations/simulations due to heterogeneous subsurface properties.

Building from our works, improved SM observations are needed in data sparse regions to validate the identified regime shifts, impact assessments must incorporate changing hydroclimatic interdependence to avoid misestimating losses, and adaptation in highly exposed agricultural regions, especially the NSZ, should be guided by the identified shifts such as the SM to Pr sign reversal, the emergence of E as a co-dominant driver, and the $P - E$ imbalance that collectively reshape water availability for rainfed systems. As warming continues, accurately assessing the evolving hydroclimatic interdependencies are critical for improving projections of global water and crop sustainability.

3 Methods

3.1 Datasets

The Coupled Model Intercomparison Project Phase 6 (CMIP6)[31] are obtained via the CMIP6 data portal (https://esgf-node.llnl.gov/search/cmip6/). Five CMIP6 models (MIROC6, NorESM2-LM, NorESM2-MM, CMCC-CM2-SR5, and CMCC-ESM2) are examined for *early-*, *mid-* and the *end of century* projections, while the European Centre for Medium-Range Weather Forecasts Reanalysis v5 (ERA5) reanalysis dataset

[38] are examined for *early century* period. Models and reanalysis data are selected based on the availability of datasets. Since no single model persistently deviates most from the ensemble across all temporal, spatial, and variable domains, therefore, we cannot decide which models perform better of worse. Therefore, we include all models in the analysis and focus on identifying patterns that are most consistently agreed upon across models.

CMIP6 datasets were analysed at their native grid spacings (100–250 km, depending on the model), while ERA5 data ($0.25° \times 0.25°$) were bilinearly interpolated to $1° \times 1°$ resolution for consistency with most CMIP6 datasets. We use the first ensemble member ("r1i1p1f1") for the CMIP6 variables include mean near-surface air temperature (*tas*,K), precipitable water (*prw*, $\mathrm{kg\,m^{-2}}$), precipitation (*pr*, $\mathrm{kg/m^2/s}$), evaporation (derived from surface upward latent heat flux, *hfls*, $\mathrm{W/m^2}$), total soil moisture content (*mrsos*, $\mathrm{kg/m^2}$), and surface runoff (*mrro*, $\mathrm{kg/m^2/s}$). Corresponding ERA5 variables are 2m temperature (*t2m*, air temperature (*tas*), K), total column water vapor (*tcwv*, $\mathrm{kg\,m^{-2}}$), total precipitation (*tp*, m), evaporation (*e*, m), soil moisture (*swvl1*, $\mathrm{m^3/m^3}$), and runoff (*ro*, m). All CMIP6 variables were analyzed at daily resolution, except for *prw* from the CMCC-CM2-SR5 and CMCC-ESM2, which are monthly due to quality concerns in the daily outputs [64]. Units for Pr, E, and q were standardized in millimetres per day (mm/day). Prw in millimetres (mm), while SM in ($\mathrm{m^3/m^3}$). For T, we report *absolute changes* in °C, while *relative changes* are calculated on a Kelvin basis. Annual and seasonal datasets were constructed by averaging daily values of T, prw, and SM, whereas Pr, E, and q were aggregated by summation.

Administrative country-level delineation obtained from https://gadm.org/ and rice and maize datasets obtain from FAOSTAT: Food and Agriculture Organization of the United Nations Statistics Division (https://www.fao.org/faostat/en/). We selected *early century* period (1981–2010) for comparison based on historical data availability. In addition, GDP projections are taken from Wang and Sun (2022)[65], which estimates high-resolution gridded datasets using nighttime light downscaling.

3.2 IPCC's temperature thresholds

Considering the lack of observational records during pre-industrial periods, as a benchmark, we define thresholds (t_h) at 1.5°C and 2.0°C warming from the increase in global mean temperature from the pre-industrial period 1850–1900 (t_0), which aligns with the definition used in the IPCC's Fifth Assessment Report (AR5) [66], to the modern baseline period of 1971–2000 (t_x).

$$t_{h1.5} = 1.5 - (t_x - t_0) \tag{1}$$

$$t_{h2.0} = 2.0 - (t_x - t_0) \tag{2}$$

While the warming from pre-industrial levels to the baseline decade is estimated at approximately 0.3°C, the thresholds for $t_{h\,1.5}$ and $t_{h\,2.0}$ correspond to global mean temperature increases of 1.2°C and 1.7°C, respectively.

3.3 Sensitivity of hydroclimatic variables

The selection of baseline period of 1971–2000[60] is supported by the absence of satellite data in ERA5 prior to 1970, during which the reanalysis relied exclusively on sparse in-situ observations, particularly over the Southern Hemisphere[38]. The period 1981–2010 was chosen to represent the historical interval in CMIP6, consistent with the standard separation between historical and future simulations [67].

The variable change (VC) was calculated as the difference in mean values between the target and baseline periods, defined as $VC = \overline{X} - \overline{B}$, where VC denotes the variable change, $\overline{X}$ is the mean value for the target period (*early-*, *mid-*, and *end of century*), and $\overline{B}$ is the mean value for the baseline period.

Global mean surface temperature (GMST) and regional mean surface temperature (RMST) are analyzed separately as they reflect fundamentally distinct mechanisms. GMST operates at the planetary scale and is governed by a thermodynamically constrained balance between radiative forcings[68], radiative response[6] and ocean heat uptake[9]. In contrast, RMST emerges from the spatial redistribution of energy through atmospheric and ocean circulation, modulated by land–sea contrasts[68], and land–atmosphere feedbacks[16, 18]. Accordingly, we report mean changes of model projection to GMST in natural units to provide interpretable metrics for policymakers, whereas express mean and variance changes for the ensemble behaviour in percentage to ensure unit consistency among hydroclimatic variables.

3.4 Consistency check of CMIP6 to ERA5 reanalysis data and intermodel comparison

Overall, both annual and seasonal changes from CMIP6 models are consistent with ERA5, although in approximately half of simulations, ERA5 slightly underestimates the magnitude of mean shifts in hydroclimatic variables. Across most regions, ERA5 exhibits lower temperature shifts at seasonal timescales, whereas annual shifts are comparable (Fig. S1a,d,g Supplementary 6). The most pronounced gap occurs in precipitable water at both annual and seasonal scales, with the largest discrepancies across regions observed during JJA and DJF, when CMIP6 deviates from ERA5 by 0.22 ± 0.15 mm and 0.14 ± 0.05 mm, respectively (Fig. S2a,d,g Supplementary 6). These results indicate that hydroclimatic dynamics of atmospheric variables are more pronounced at the seasonal timescale. The most consistent shifts show by precipitation at both annual and seasonal scales (Fig. S3a,d,g Supplementary 6), while by contrast, evaporation shows more distinct behavior, with shifts in ERA5 exceeding CMIP6 at the annual scale but becoming uniformly negative at seasonal periods (Fig. S4a,d,g Supplementary 6). The $P - E$ disentangling here should be interpreted with caution, especially when assessing water availability, as these results imply greater uncertainty in evaporation[69] than in precipitation. Furthermore, for soil moisture and runoff, ERA5 values are generally lower than CMIP6 projections at the annual scale, while their seasonal responses are comparable (Fig. S5a,d,g and Fig. S6a,d,g Supplementary 6), indicating the uncertainty linked to spring and autumn seasons. Despite moderate discrepancies in magnitude[10, 43], the broad consistency between CMIP6 and

ERA5 supports the use of CMIP6 for diagnosing hydroclimatic responses to warming in future scenarios.

Among the five CMIP6 models, CMCC-CM2-SR5 exhibits the strongest responses in T, prw, and Pr (Fig. 2; Fig. S1-2 Supplementary 1), CMCC-ESM2 in E (Fig. S3 Supplementary 1), and CMCC-ESM2 and NorESM-LM in SM and q (Fig. S4-5 Supplementary 1), likely due to differences in thermodynamic parameterizations[64, 70, 71].

3.5 Granger Causality

We employed Granger causality[72] analysis to identify causal networks between hydroclimatic variables. Prior to the analysis, we verified the stationarity of the time series by testing the null hypothesis using the Augmented Dickey–Fuller (ADF) regression on the projection datasets (2021–2050 and 2071–2100).

$$\Delta X_t = \alpha + \beta t + \gamma X_{t-1} + \sum_{i=1}^{p} \delta_i \, \Delta X_{t-i} + \varepsilon_t \tag{3}$$

where $\Delta X_t = X_t - X_{t-1}$, and we reject non-stationarity when the ADF p-value $< \alpha = 0.05$ (i.e., $\gamma < 0$ significantly). If the ADF p-value exceeds α, we difference the series and apply the results to develop the autoregressive and full variables:

$$X_t^{(1)} = X_t - X_{t-1}. \tag{4}$$

To conduct causality analysis, a bivariate model between two stationary time series is estimated:

$$Y_t = \sum_{j=1}^{m} a_j Y_{t-j} + \sum_{j=1}^{m} b_j X_{t-j} + \varepsilon_t \tag{5}$$

$$X_t = \sum_{j=1}^{m} c_j X_{t-j} + \sum_{j=1}^{m} d_j Y_{t-j} + \eta_t \tag{6}$$

Failure to reject the null hypothesis of non-causality for certain variable pairs indicates no evidence of predictive causality in these directions. We classified causality into three levels: strong ($p < 0.001$), moderate ($0.001 < p < 0.01$), and weak ($0.01 < p < 0.05$)[73]. Values exceeding 0.05 were considered not statistically significant, indicating no detectable causality.

3.6 Random Forest with SHAP

We translate the RF–SHAP framework to an intermediate level of model explainability, in which relationships are clustered by driver and target variables and characterized based on their dependencies and directional effects. In particular, RF–SHAP attributes feature contributions by averaging over conditional expectations across all feature coalitions, accounting for both positive and negative effects [27, 74, 75]. Within the RF–SHAP framework, a positive predictive influence (upward) indicates that

source variable increase prediction of the target variable, whereas a negative predictive influence (downward) indicates that source variable limits the target response[76].

We build lagged features as:

$$\mathcal{A}_t = [T_{t-1},\, T_{t-2},\, T_{t-3},\, T_{t-4}], \tag{7}$$

$$\mathcal{F}_t = \left\{V_{j,t},\, V_{j,t-1},\, V_{j,t-2}\right\}_{j=1}^{5}, \tag{8}$$

$$\mathbf{X}_t^{\text{base}} = \mathcal{A}_t, \qquad \mathbf{X}_t^{\text{full}} = [\,\mathcal{A}_t \parallel \mathcal{F}_t\,]. \tag{9}$$

where T_t denote the target (e.g., runoff) and V_t^i the i-th source variable (e.g., temperature, precipitable water, precipitation, evaporation, soil moisture), with $t = 1, \ldots, N$ at annual or seasonal resolution.

AR lags were set to 4 and feedback lags to 2 to capture short-term dependencies while limiting overfitting given 30-season samples [77, 78].

We estimate:

$$\hat{T}_t^{\text{base}} = f_{\text{RF, base}}\big(\mathbf{X}_t^{\text{base}}\big), \qquad \hat{T}_t^{\text{full}} = f_{\text{RF, full}}\big(\mathbf{X}_t^{\text{full}}\big), \tag{10}$$

with Random Forests of 200 trees (maximum depth 3) to capture nonlinearity without instability and apply moving block bootstrap resampling (n=1000)[79]. We compute the test R^2 as

$$R^2_{\text{base}} = 1 - \frac{\sum_{t\in\mathcal{S}_{\text{test}}} \left(T_t - \hat{T}_t^{\text{base}}\right)^2}{\sum_{t\in\mathcal{S}_{\text{test}}} \left(T_t - \bar{T}_{\text{test}}\right)^2}, \tag{11}$$

$$R^2_{\text{full}} = 1 - \frac{\sum_{t\in\mathcal{S}_{\text{test}}} \left(T_t - \hat{T}_t^{\text{full}}\right)^2}{\sum_{t\in\mathcal{S}_{\text{test}}} \left(T_t - \bar{T}_{\text{test}}\right)^2}. \tag{12}$$

where $\mathcal{S}_{\text{test}}$ denote the index set of samples in the held-out test split, $\bar{T}_{\text{test}} = |\mathcal{S}_{\text{test}}|^{-1}\sum_{t\in\mathcal{S}_{\text{test}}} T_t$. To stabilize performance, we report robust R^2 as the average across cross-validation folds [80].

For each target T_j (index j is hydroclimatic variables), feedback strength is:

$$\Delta R^2_{T_j} \equiv R^2_{\text{full}} - R^2_{\text{base}}, \qquad \text{FeedbackStrength}_{T_j} = \max\big(0,\, \Delta R^2_{T_j}\big). \tag{13}$$

Negative values of ΔR^2_T, which may arise from sampling variability or weak predictors, are set to zero to ensure that feedback strength reflects only additional explanatory power beyond autoregressive memory. Across targets within a region, we apply min–max normalization:

$$\Delta R^{2,\text{norm}}_T = \begin{cases} \dfrac{\Delta R^2_T - \min_T \Delta R^2_T}{\max_T \Delta R^2_T - \min_T \Delta R^2_T}, & \text{if } \max \neq \min, \\ 0.5, & \text{otherwise.} \end{cases} \tag{14}$$

We report two complementary importances. First, impurity-based RF importance

$$I_k = \sum_{\text{trees}} \sum_{\text{splits on } k} \frac{n_{\text{split}}}{n_{\text{root}}} \Delta\text{Impurity}, \tag{15}$$

where ΔImpurity is the decrease in node variance (regression). Second, SHAP values $\phi_{k,t}$ measure the relative additive contribution of feature k at sample t[74, 75]. From these we compute: (i) global feature importance,

$$S_k = \mathbb{E}_t[\,|\phi_{k,t}|\,], \tag{16}$$

(ii) variable-level dependency for source variable V quantified the contribution of each climate variable to predicting other variables using SHAP values, where the mean is taken across all testing samples. This metric aggregates the contribution from the current value and two lagged values of variable "V" to Random Forest predictions $\mathcal{K}(V) = \{V_t, V_{t-1}, V_{t-2}\}$,

$$D_V = \mathbb{E}_t \left[\sum_{k \in \mathcal{K}(V)} |\phi_{k,t}| \right], \tag{17}$$

and (iii) directional effect,

$$E_V = \mathbb{E}_t \left[\sum_{k \in \mathcal{K}(V)} \phi_{k,t} \right]. \tag{18}$$

These metrics distinguish which predictors matter, how whole variables contribute, and whether their net influence is positive or negative, with qualitatively contribution level interpretation[54]. We defined the contribution levels as strong ($D_V > 0.03$), medium ($D_V > 0.02$), and weak ($D_V > 0.015$). Values below 0.015 indicate no detectable dependency.

Network Change

We modeled interactions among variables as a directed-weighted graph. For each period t, we constructed an adjacency matrix $\mathbf{A}^{(t)} \in \mathbb{R}^{6\times6}$ whose entry $A_{ij}^{(t)}$ quantifies the directed influence from source variable i to target variable j and removes self-loops. We produced two versions of $\mathbf{A}^{(t)}$, namely GC and RF-SHAP dependency. To quantify temporal reconfiguration, we compared the early network $\mathbf{A}^{(1)}$ (2021–2050) with the late network $\mathbf{A}^{(2)}$ (2071–2100). We defined binary presence masks:

$$\mathbf{B}^{(t)} = \mathbb{I}\Big(|\mathbf{A}^{(t)}| > \tau\Big) \tag{19}$$

and classified edges as new, lost, or stable according to their presence across periods, that is, new when $B_{ij}^{(1)} = 0$, $B_{ij}^{(2)} = 1$; lost when $B_{ij}^{(1)} = 1$, $B_{ij}^{(2)} = 0$; and stable when $B_{ij}^{(1)} = B_{ij}^{(2)} = 1$. For stable, non–sign-flipping edges, we quantified strength change by the relative difference

$$\Delta_{ij} \;=\; \frac{|A_{ij}^{(2)}| - |A_{ij}^{(1)}|}{|A_{ij}^{(1)}|}, \tag{20}$$

labeling edges as *strengthened* if $\Delta_{ij} > 0.1$ and *weakened* if $\Delta_{ij} < -0.1$. We also report the raw difference matrix:

$$\mathbf{D} \;=\; \mathbf{A}^{(2)} - \mathbf{A}^{(1)}, \tag{21}$$

To establish a consistent network structure across both GC and RF–SHAP, we apply threshold criteria of $p < 0.05$ for GC and $\mathrm{D}_V > 0.015$ for RF-SHAP, enabling the identification of minor yet statistically robust connections and the delineation of both positive and negative predictive influence directions.

3.7 Projecting impact of shifts in hydroclimatic variable to yield variance

To quantify the influence of hydroclimatic variables on food production, we employ an empirical modeling framework based on restricted cubic splines (RCS)[81]. Widely applied in medical studies, this approach effectively captures nonlinear and continuous relationships between the response variable and multiple predictors[29, 81, 82].

$$Y_{it} = f_E(E_{it}) + f_{SM}(SM_{it}) + \lambda_i + \alpha_i t + \epsilon_{it} \tag{22}$$

where Y_{it} are log yields in region i during year t; f_E and f_{SM} are coefficients describing marginal effects of E and SM; E_{it} and SM_{it} are dominant drivers; λ_i and $\alpha_i t$ are effects of E and SM; and ϵ_{it} is unexplained variations which not explained by E, SM, and the spatiotemporal effects of E and SM, such as T and other non-dominant drivers in the system.

We define yield productivity as crop yield per unit harvested area, thereby isolating changes in production from expansion/reduction of cropland area.

3.8 Projecting GDP impact

To translate the effect of yield variance into GDP, we use empirical dose–response functions method [30] by comparing *end of century* both agricultural productivity and GDP under high emission scenario to a *early century* period, for consistency with the calculation of impact in yield variance. Due to data limitation, the baseline is represented by the year 2005, used as a proxy for the 1981–2010 climatology, while *end of century* conditions are represented by the mean over selected future years (2070, 2080, 2090, and 2100)[65], corresponding to the period 2071–2100.

For each country c, baseline gross domestic product (GDP) G_c^{base} and baseline crop yields for rice and maize, $Y_c^{(r)\mathrm{base}}$ and $Y_c^{(m)\mathrm{base}}$, are extracted for the baseline year. *End of century* GDP and yields are computed as arithmetic means over the projection years,

$$\bar{G}_c^{\mathrm{fut}} = \frac{1}{|T|}\sum_{t\in T} G_{c,t}, \quad \bar{Y}_c^{(r)\mathrm{fut}} = \frac{1}{|T|}\sum_{t\in T} Y_{c,t}^{(r)}, \quad \bar{Y}_c^{(m)\mathrm{fut}} = \frac{1}{|T|}\sum_{t\in T} Y_{c,t}^{(m)}, \tag{23}$$

where $T = \{2070, 2080, 2090, 2100\}$.

Percentage yield changes between the baseline and *end of century* period are calculated separately for rice and maize,

$$\Delta Y_c^{(r)}(\%) = \frac{\bar{Y}_c^{(r)\text{fut}} - Y_c^{(r)\text{base}}}{Y_c^{(r)\text{base}}} \times 100, \quad \Delta Y_c^{(m)}(\%) = \frac{\bar{Y}_c^{(m)\text{fut}} - Y_c^{(m)\text{base}}}{Y_c^{(m)\text{base}}} \times 100. \tag{24}$$

An aggregate yield change is then defined as the equally weighted mean of rice and maize yield changes,

$$\Delta Y_c^{\text{comb}}(\%) = 0.5\,\Delta Y_c^{(r)}(\%) + 0.5\,\Delta Y_c^{(m)}(\%). \tag{25}$$

To translate yield changes into macroeconomic exposure, we apply a constant yield-GDP elasticity η, set to -0.1, such that the percentage GDP impact attributable to yield change reflects that agriculture is typically about 10% of GDP in many countries, so a 1% yield change translates to roughly 0.1% GDP change, following Waidelich et.al (2024)[30] is

$$\Delta G_c(\%) = \eta \cdot \Delta Y_c^{\text{comb}}(\%). \tag{26}$$

The absolute GDP exposed to yield risk is then computed as the magnitude of this impact applied to *end of century* GDP,

$$G_c^{\text{risk}} = \bar{G}_c^{\text{fut}} \times \frac{|\Delta G_c(\%)|}{100}. \tag{27}$$

Supplementary information. Supplementary data and table are provided in Extended Data and Supplementary Table.

Acknowledgements. This work was supported by the Indonesian Education Scholarship, Center of Higher Education Funding and Assessment, and Indonesian Endowment Fund for Education.

Contribution. D.I. conceived the idea and designed the problem. D.I., S.M., and A.R.G. designed the solution. D.I. wrote the code and performed the analysis. D.I. and S.M. analysed the results. D.I. wrote the first draft in collaboration with S.M. with advices from P.G. and A.R.G. who reviewed the manuscript.

References

[1] Douville, H., Raghavan, K., Renwick, J., Allan, R.P., Arias, P.A., Barlow, M., Cerezo-Mota, R., Cherchi, A., Gan, T.Y., Gergis, J., Jiang, D., Khan, A., Mba, W.P., Rosenfeld, D., Tierney, J., Zolina, O.: 2021: Water Cycle Changes. In Climate Change 2021: The Physical Science Basis. Contribution of Working Group I to the Sixth Assessment Report of the Intergovernmental Panel on Climate Change. Cambridge University Press, Cambridge, UK and New York, NY, USA (2021)

[2] Ravinandrasana, V.P., Franzke, C.L.E.: The first emergence of unprecedented global water scarcity in the anthropocene. Nature Communications **16** (2025) https://doi.org/10.1038/s41467-025-63784-6

[3] NOAA National Centers for Environmental Information (NCEI): U.S. Billion-Dollar Weather and Climate Disasters. Accessed: 2026-01-05 https://www.ncei.noaa.gov/access/billions (2026)

[4] Müller, O.V., McGuire, P.C., Vidale, P.L., Hawkins, E.: River flow in the near future: a global perspective in the context of a high-emission climate change scenario. HESS **28**, 2179–2024 (2024) https://doi.org/10.5194/hess-28-2179-2024

[5] Wing, O.E.J., Bates, P.D., Quinn, N.D., Savage, J.T.S., Uhe, P.F., Cooper, A., Collings, T.P., Addor, N., Lord, N.S., Hatchard, S., Hoch, J.M., Bates, J., Probyn, I., Himsworth, S., González, J.R., Brine, M.P., Wilkinson, H., Sampson, C.C., Smith, A.M., Neal, J.C., Haigh, I.D.: A 30 m global flood inundation model for any climate scenario. Water Researches Research **60**, 2023–036460 (2024) https://doi.org/10.1029/2023WR036460

[6] Kim, S.-K., Shin, J., An, S.-I., Kim, H.-J., Im, N., Xie, S.-P., Kug, J.-S., Yeh, S.-W.: Widespread irreversible changes in surface temperature and precipitation in response to CO2 forcing. Nature Climate Change **12**, 834–840 (2022) https://doi.org/10.1038/s41558-022-01452-z

[7] Hsu, H., Dirmeyer, P.A.: Nonlinearity and multivariate dependencies in the terrestrial leg of land-atmosphere coupling. Water Resources Research **57**(2), 2020–028179 (2021) https://doi.org/10.1029/2020WR028179

[8] Lin, X., Huang, S., Li, J., Huang, Q., Shi, H., She, D., Leng, G., Wei, X., Guo, W., Liu, Y., Luo, J.: Feedback dynamics between precipitation, temperature, and soil moisture in china and their possible driving mechanisms under a changing environment. Atmospheric Research **294** (2023) https://doi.org/10.1016/j.atmosres.2023.106983

[9] Kang, S.M., Ceppi, P., Yu, Y., Kang, I.-S.: Recent global climate feedback controlled by Southern Ocean cooling. Nature Geoscience **16**, 775–780 (2023) https://doi.org/10.1038/s41561-023-01256-6

[10] Allen, M.R., Ingram, W.J.: Constraints on future changes in climate and the hydrologic cycle. Nature **419**, 224–232 (2002) https://doi.org/10.1038/nature01092

[11] Held, I.M., Soden, B.J.: Robust responses of the hydrological cycle to global warming. Journal of Climate **19**, 5686–5699 (2006) https://doi.org/10.1175/JCLI3990.1

[12] Gu, B., Zhou, S., Yu, B., Findell, K.L., Lintner, B.R.: Multifaceted changes in

water availability with a warmer climate. npj Climate and Atmospheric Science **8** (2025) https://doi.org/10.1038/s41612-025-00913-4

[13] Meyer, M., Strulovici, B.: Beyond Correlation: Measuring Interdependence Through Complementarities (2013)

[14] Turner, S.W.D., Voisin, N., Fazio, J., Hua, D., Jourabchi, M.: Compound climate events transform electrical power shortfall risk in the pacific northwest. Nature Communications **10** (2019) https://doi.org/10.1038/s41467-018-07894-4

[15] Zhou, S., Williams, A.P., Berg, A.M., Gentine, P.: Land–atmosphere feedbacks exacerbate concurrent soil drought and atmospheric aridity. PNAS **116**, 18848–18853 (2019) https://doi.org/10.1073/pnas.1904955116

[16] Seneviratne, S.I., Lüthi, D., Litschi, M., Schär, C.: Land–atmosphere coupling and climate change in europe. Nature **443**, 205–209 (2006) https://doi.org/10.1038/nature05095

[17] Cael, B.B., Bloch-Johnson, J., Ceppi, P., Fredriksen, H.-B., Goodwin, P., Gregory, J.M., Smith, C.J., Williams, R.G.: Energy budget diagnosis of changing climate feedback. Science Advances **9** (2023) https://doi.org/10.1126/sciadv.adf9302

[18] Humphrey, V., Berg, A., Ciais, P., Gentine, P., Jung, M., Reichstein, M., Seneviratne, S.I., Frankenberg, C.: Soil moisture–atmosphere feedback dominates land carbon uptake variability. Nature **592**, 65–69 (2021) https://doi.org/10.1038/s41586-021-03325-5

[19] Alessi, M.J., Herrera, D.A., Evans, C.P., DeGaetano, A.T., Ault, T.R.: Soil moisture conditions determine land-atmosphere coupling and drought risk in the northeastern united states. JGR Atmospheres **127**, 2021–034740 (2022) https://doi.org/10.1029/2021JD034740

[20] Ghajarnia, N., Kalantari, Z., Orth, R., Destouni, G.: Close co-variation between soil moisture and runoff emerging from multi-catchment data across Europe. Scientific Reports **10** (2020) https://doi.org/10.1038/s41598-020-61621-y

[21] Mahan, K., Mizera, M.: Warm temperatures break decade-old records across New England, century-old record in Boston. Accessed: 2026-04-13 https://www.bostonglobe.com/2026/03/09/metro/new-england-forecast-warm-weather/ (2026)

[22] Hsu, H., Dirmeyer, P.A.: Soil moisture-evaporation coupling shifts into new gears under increasing CO2. Nature Communications **14** (2023) https://doi.org/10.1038/s41467-023-36794-5

[23] Sun, J., Yang, K., He, X., Wang, G., Wang, Y., Yu, Y., Lu, H.: Causal pathways underlying global soil moisture–precipitation coupling. Nature Communications

16 (2025) https://doi.org/10.1038/s41467-025-63999-7

[24] Rao, X., Zhang, J., Chen, T.: Coupling of land surface thermodynamics with atmospheric dynamics effect on summer extreme precipitation in the northern tibetan plateau. Journal of Geophysical Research: Atmospheres **130**(21), 2025–044632 (2025)

[25] Seneviratne, S.I., Corti, T., Davin, E.L., Hirschi, M., Jaeger, E.B., Lehner, I., Orlowsky, B., Teuling, A.J.: Investigating soil moisture–climate interactions in a changing climate: A review. Earth-Science Reviews **99**, 125–161 (2010) https://doi.org/10.1016/j.earscirev.2010.02.004

[26] Sugihara, G., May, R., Ye, H., Hsieh, C.-h., Deyle, E., Fogarty, M., Munch, S.: Detecting causality in complex ecosystems. Science **338**, 496–500 (2012) https://doi.org/10.1126/science.1227079

[27] Castro, M., Júnior, P.R.M., Soriano-Vargas, A., Oliveira Werneck, R., Gonçalves, M.M., Filho, L.L., Moura, R., Zampieri, M., Linares, O., Ferreira, V., Ferreira, A., Davólio, A., Schiozer, D., Rocha, A.: Time series causal relationships discovery through feature importance and ensemble models. Scientific Reports **13** (2023) https://doi.org/10.1038/s41598-023-37929-w

[28] Lundberg, S., Lee, S.-I.: A Unified Approach to Interpreting Model Predictions. Preprint at https://doi.org/10.48550/arXiv.1705.07874 (2017)

[29] Proctor, J., Zeppetello, L.V., Chan, D., Huybers, P.: Climate change increases the interannual variance of summer crop yields globally through changes in temperature and water supply. Science Advances **11** (2025) https://doi.org/10.1126/sciadv.ady3575

[30] Waidelich, P., Batibeniz, F., Rising, J., Kikstra, J.S., Seneviratne, S.I.: Climate damage projections beyond annual temperature. Nature Climate Change **14**, 592–599 (2024) https://doi.org/10.1038/s41558-024-01990-8

[31] Eyring, V., Bony, S., Meehl, G.A., Senior, C.A., Stevens, B., Stouffer, R.J., Taylor, K.E.: Overview of the coupled model intercomparison project phase 6 (CMIP6) experimental design and organization. Geoscientific Model Development **9**, 1937–1958 (2016) https://doi.org/10.5194/gmd-9-1937-2016

[32] O'Neill, B.C., Tebaldi, C., Vuuren, D.P., Eyring, V., Pierre Friedlingstein, G.H., Knutti, R., Kriegler, E., Lamarque, J.-F., Lowe, J., Meehl, G.A., Moss, R., Riahi, K., Sanderson, B.M.: The Scenario Model Intercomparison Project (ScenarioMIP) for CMIP6

[33] Ganguli, P., Majhi, A., Kumar, R.: Observational evidence for multivariate drought hazard amplifications across disparate climate regimes. Earth's Future **10**, 2022–002809 (2022) https://doi.org/10.1029/2022EF002809

[34] Najibi, N., Devineni, N.: Recent trends in the frequency and duration of global floods. Earth System Dynamics **9**, 757–783 (2018) https://doi.org/10.5194/esd-9-757-2018

[35] Aguado, E., Burt, J.E.: Understanding Weather and Climate. Pearson, Boston (2018)

[36] Zhai, J., Boos, W.: Regime transitions of cross-equatorial Hadley circulations with zonally asymmetric thermal forcings. Journal of the Atmospheric Sciences **72**, 3800–3818 (2015) https://doi.org/10.1175/JAS-D-15-0025.1

[37] Pörtner, H.-O., Roberts, D.C., Tignor, M., Poloczanska, E.S., Mintenbeck, K., Alegría, A., Craig, M., Langsdorf, S., Löschke, S., Möller, V., Okem, A., Rama, B. (eds.): Climate Change 2022: Impacts, Adaptation and Vulnerability. Cambridge University Press, Cambridge, UK (2022)

[38] Hersbach, H., Bell, B., Berrisford, P., Hirahara, S., Horányi, A., Muñoz-Sabater, J., Nicolas, J., Peubey, C., Radu, R., Schepers, D., Simmons, A., Soci, C., Abdalla, S., Abellan, X., Balsamo, G., Bechtold, P., Biavati, G., Bidlot, J., Bonavita, M., Chiara, G.D., Dahlgren, P., Dee, D., Diamantakis, M., Dragani, R., Flemming, J., Forbes, R., Fuentes, M., Geer, A., Haimberger, L., Healy, S., Hogan, R.J., Hólm, E., Janisková, M., Keeley, S., Laloyaux, P., Lopez, P., Lupu, C., Radnoti, G., Rosnay, P., Rozum, I., Vamborg, F., Villaume, S., Thépaut, J.-N.: The ERA5 global reanalysis. Quarterly Journal of the Royal Meteorological Society **146**, 1999–2049 (2020) https://doi.org/10.1002/qj.3803

[39] Byrne, M.P., O'Gorman, P.A.: Land–ocean warming contrast over a wide range of climates: Convective quasi-equilibrium theory and idealized simulations. Journal of Climate **26**, 4000–4016 (2013) https://doi.org/10.1175/JCLI-D-12-00262.1

[40] Xu, Y., Ramanathan, V.: Latitudinally asymmetric response of global surface temperature: Implications for regional climate change. Geophysical Research Letters **39** (2012) https://doi.org/10.1029/2012GL052116

[41] Peixoto, J.P., Oort, A.: Physics of Climate. Springer, New York (1992)

[42] Feulner, G., Rahmstorf, S., Levermann, A., Volkwardt, S.: On the origin of the surface air temperature difference between the hemispheres in Earth's present-day climate. Journal of Climate **26**, 7136–7150 (2013) https://doi.org/10.1175/JCLI-D-12-00636.1

[43] Wentz, F.J., Ricciardulli, L., Hilburn, K., Mears, C.: How much more rain will global warming bring? Science **317**, 233–235 (2007) https://doi.org/10.1126/science.1140746

[44] Liu, Q., Grassotti, C., Zhou, Y., Lee, Y.-K., Liu, S., Yang, J.X.: Trends of

temperature and total precipitable water, as well as the trend of surface pressure induced by CO2. Scientific Reports **14** (2024) https://doi.org/10.1038/s41598-024-80685-8

[45] Grise, K.M., Davis, S.M.: Hadley cell expansion in CMIP6 models. Atmospheric Chemistry and Physics **20**, 5249–5268 (2020) https://doi.org/10.5194/acp-20-5249-2020

[46] Schmidt, D.F., Grise, K.M.: The response of local precipitation and sea level pressure to Hadley cell expansion. Geophysical Research Letters **44** (2017) https://doi.org/10.1002/2017GL075380

[47] Qing, Y., Wang, S., Yang, Z.-L., Gentine, P., Zhang, B., Alexander, J.: Accelerated soil drying linked to increasing evaporative demand in wet regions. npj Climate and Atmospheric Science **26** (2023) https://doi.org/10.1038/s41612-023-00531-y

[48] Zhou, S.: Land surface processes are the dominant driver of global runoff increase. Nature Climate Change **13**, 426–427 (2023) https://doi.org/10.1038/s41558-023-01666-9

[49] Wasko, C., Sharma, A., Lettenmaier, D.P.: Increases in temperature do not translate to increased flooding. Nature Communications **10** (2019) https://doi.org/10.1038/s41467-019-13612-5

[50] Mondal, S., Mishra, A.: Quantifying the precipitation, evapotranspiration, and soil moisture network's interaction over global land surface hydrological cycle. Water Resources Research **60**, 2023–034861 (2024) https://doi.org/10.1029/2023WR034861

[51] Donges, J.F., Zou1, Y., Marwan, N., Kurths, J.: Complex networks in climate dynamics. The European Physical Journals **174**, 157–179 (2009) https://doi.org/10.1140/epjst/e2009-01098-2

[52] Chen, D., Chen, J., Zhang, X., Jia, Q., Liu, X., Sun, Y., Lü, L., Yu, W.: Critical Nodes Identification in Complex Networks: A Survey. Preprint at https://doi.org/10.48550/arXiv.2507.06164 (2025)

[53] Runge, J., Nowack, P., Kretschmer, M., Flaxman, S., Sejdinovic, D.: Detecting and quantifying causal associations in large nonlinear time series datasets. Science Advances **5** (2019) https://doi.org/10.1126/sciadv.aau4996

[54] Lundberg, S.M., Erion, G., Chen, H., DeGrave, A., Prutkin, J.M., Nair, B., Katz, R., Himmelfarb, J., Bansal, N., Lee, S.-I.: From local explanations to global understanding with explainable AI for trees. Nature Machine Intelligence **2**, 56–67 (2020) https://doi.org/10.1038/s42256-019-0138-9

[55] Mcgraw, M.C., Barnes, E.A.: Memory matters: A case for granger causality in climate variability studies. Journal of Climate **31**, 3289–3300 (2018) https://doi.org/10.1175/JCLI-D-17-0334.1

[56] Fujita, M., Sato, T.: Observed behaviours of precipitable water vapour and precipitation intensity in response to upper air profiles estimated from surface air temperature. Scientific Reports **7** (2017) https://doi.org/10.1038/s41598-017-04443-9

[57] Song, Y.M., Wang, Z.F., Qi, L.L., Huang, A.N.: Soil moisture memory and its effect on the surface water and heat fluxes on seasonal and interannual time scales. JGR Atmosphere **124**, 10730–10741 (2019) https://doi.org/10.1029/2019JD030893

[58] Chen, Q., Li, W., Tan, L., Tian, F.: Harnessing knowledge from maize and rice domestication for new crop breeding. Molecular Plant **14**, 9–26 (2021) https://doi.org/10.1016/j.molp.2020.12.006

[59] Food, United Nations, A.O.: FAOSTAT: Commodities by regions. Accessed: 2026-04-07 https://www.fao.org/faostat/en/#rankings/commodities_by_regions (2024)

[60] Konapala, G., Mishra, A.K., Wada, Y., Mann, M.E.: Climate change will affect global water availability through compounding changes in seasonal precipitation and evaporation. Nature Communications **11** (2020) https://doi.org/10.1038/s41467-020-16757-w

[61] Tigchelaar, M., Battisti, D.S., Naylor, R.L., , Ray, D.K.: Future warming increases probability of globally synchronized maize production shocks. PNAS **115**, 6644–6649 (2018) https://doi.org/10.1073/pnas.171803111

[62] Proctor, J., Rigden, A., Chan, D., Huybers, P.: More accurate specification of water supply shows its importance for global crop production. Nature food **3**, 753–763 (2022) https://doi.org/10.1038/s43016-022-00592-x

[63] Sun, W., Zhou, S., Yu, B., Zhang, Y., Keenan, T., Fu, B.: Soil moisture-atmosphere interactions drive terrestrial carbon-water trade-offs. Communications Earth Environment **6** (2025) https://doi.org/10.1038/s43247-025-02145-z

[64] Lovato, T., Peano, D., Butenschön, M., Materia, S., Iovino, D., Scoccimarro, E., Fogli, P.G., Cherchi, A., Bellucci, A., Gualdi, S., Masina, S., Navarra, A.: CMIP6 simulations with the CMCC Earth System Model (CMCC-ESM2). Journals of Advances in Modelling Earth Systems **14**, 2021–002814 (2022) https://doi.org/10.1029/2021MS002814

[65] Wang, T., Sun, F.: Global gridded GDP data set consistent with the shared socioeconomic pathways. Scientific Data **221** (2022) https://doi.org/10.1038/

s41597-022-01300-x

[66] Allen, M.R., Dube, O.P., Solecki, W., Aragón-Durand, F., Cramer, W., Humphreys, S., Kainuma, M., Kala, J., Mahowald, N., Mulugetta, Y., Perez, R., Wairiu, M., Zickfeld, K.: Framing and Context. Cambridge University Press, Cambridge, UK and New York, NY, USA (2018)

[67] Szalkai, Z., Kristóf, E., Zsákai, A., Ács, F.: Comparison of CMIP6 model performance in estimating human thermal load in Europe in the winter season. International Journal of Climatology **44**, 3328–3341 (2024) https://doi.org/10.1002/joc.8526

[68] Seneviratne, S.I., Donat, M.G., Pitman, A.J., Knutti, R., Wilby, R.L.: Allowable CO2 emissions based on regional and impact-related climate targets. Nature **529**, 477–483 (2016) https://doi.org/10.1038/nature16542

[69] Miralles, D.G., Bonte, O., Koppa, A., Baez-Villanueva, O.M., Tronquo, E., Zhong, F., Beck, H.E., Hulsman, P., Dorigo, W., Verhoest, N.E.C., Haghdoost, S.: GLEAM4: global land evaporation and soil moisture dataset at 0.1° resolution from 1980 to near present. Scientific Data **416** (2025) https://doi.org/10.1038/s41597-025-04610-y

[70] Tatebe, H., Ogura, T., Nitta, T., Komuro, Y., Ogochi, K., Takemura, T., Sudo, K., Sekiguchi, M., Abe, M., Saito, F., Chikira, M., Watanabe, S., Mori, M., Hirota, N., Kawatani, Y., Mochizuki, T., Yoshimura, K., Takata, K., O'ishi, R., Yamazaki, D., Suzuki, T., Kurogi, M., Kataoka, T., Watanabe, M., Kimoto, M.: Description and basic evaluation of simulated mean state, internal variability, and climate sensitivity in MIROC6. Geoscientific Model Development **12**, 2727–2765 (2019) https://doi.org/10.5194/gmd-12-2727-2019

[71] Seland, Bentsen, M., Olivié, D., Toniazzo, T., Gjermundsen, A., Graff, L.S., Debernard, J.B., Gupta, A.K., He, Y.-C., Kirkevåg, A., Schwinger, J., Tjiputra, J., Aas, K.S., Bethke, I., Fan, Y., Griesfeller, J., Grini, A., Guo, C., Ilicak, M., Karset, I.H.H., Landgren, O., Liakka, J., Moseid, K.O., Nummelin, A., Spensberger, C., Tang, H., Zhang, Z., Heinze, C., Iversen, T., Schulz, M.: Overview of the Norwegian Earth System Model (NorESM2) and key climate response of CMIP6 DECK, historical, and scenario simulations. Geoscientific Model Development **13**, 6165–6200 (2020) https://doi.org/10.5194/gmd-13-6165-2020

[72] Granger, C.W.J.: Investigating causal relations by econometric models and cross-spectral methods. Econometrica **37** (1969) https://doi.org/10.2307/1912791

[73] Mosedale, T.J., Stephenson, D.B.: Granger causality of coupled climate processes: Ocean feedback on the North Atlantic oscillation. Journal of Climate **19**, 1182–1194 (2006) https://doi.org/10.1175/JCLI3653.1

[74] Lee, K., Ayyasamy, M.V., Ji, Y., Balachandran, P.V.: A comparison of explainable

artificial intelligence methods in the phase classification of multi-principal element alloys. Scientific Reports **12** (2022) https://doi.org/10.1038/s41598-022-15618-4

[75] Ibebuchi, C.C.: Uncertainty in machine learning feature importance for climate science: a comparative analysis of SHAP, PDP, and gain-based methods. Theoretical and Applied Climatology **156** (2025) https://doi.org/10.1007/s00704-025-05703-9

[76] Li, X., Zhang, S., Li, X., Zeng, J., Long, Y., Nie, B., Zhao, C.: SHAP-driven insights into multimodal data: behavior phase prediction for industrial safety applications. Scientific Reports **15** (2025) https://doi.org/10.1038/s41598-025-18889-9

[77] Bevacqua, E., Rakovec, O., Schumacher, D.L., Kumar, R., Thober, S., Samaniego, L., Seneviratne, S.I., Zscheischler, J.: Direct and lagged climate change effects intensified the 2022 European drought. Nature Geoscience **17**, 1100–1107 (2024) https://doi.org/10.1038/s41561-024-01559-2

[78] He, Z., Pan, S., Gu, X., Xu, M., Wang, M.: Study on the driving mechanism of lagged effects based on different time scales in a karst drainage basin in South China. Scientific Reports **13** (2023) https://doi.org/10.1038/s41598-023-36098-0

[79] MacKinnon, D.P., Lockwood, C.M., Williams, J.: Confidence limits for the indirect effect: Distribution of the product and resampling methods. Multivariate Behavioral Research **39**, 99–128 (2004) https://doi.org/10.1207/s15327906mbr3901_4

[80] Lausser, L., Szekely, R., Schmid, F., Maucher, M., Kestler, H.A.: Efficient cross-validation traversals in feature subset selection. Scientific Reports **12** (2022) https://doi.org/10.1038/s41598-022-25942-4

[81] Hsiang, S.: Climate econometrics. Annual Review of Resource Economics **8**, 43–75 (2016) https://doi.org/10.1146/annurev-resource-100815-095343

[82] Qin, X., Hung, J., Knuiman, M.W., Briffa, T.G., Teng, T.-H.K., Sanfilippo, F.M.: Evidence-based medication adherence among seniors in the first year after heart failure hospitalisation and subsequent long-term outcomes: a restricted cubic spline analysis of adherence-outcome relationships. Eur J Clin Pharmacol **79**, 553–567 (2023) https://doi.org/10.1007/s00228-023-03467-7